AIAA 03–3726

Preliminary DNS Database of Hypersonic Turbulent Boundary Layers

M. Pino Martin
Department of Mechanical and Aerospace Engineering
Princeton University, Princeton, NJ

33rd AIAA Fluid Dynamics Conference and Exhibit
June 22–26, 2003/Orlando, FL

Preliminary DNS Database of Hypersonic Turbulent Boundary Layers

M. Pino Martin
Department of Mechanical and Aerospace Engineering
Princeton University, Princeton, NJ

We are in the process of building a direct numerical simulation database of supersonic and hypersonic boundary layers that will be available to the scientific community. The data obtained from direct numerical simulation of Mach 4 turbulent boundary layers at Re_θ up to 9480 are presented, including different wall temperature conditions. The procedures for initializing the turbulent fields and determining the grid resolution are described. Under the proper transformation, the turbulent kinetic energy shows that the isothermal wall reduces the magnitude of the turbulence production and dissipation mechanisms. The presence of shock waves is illustrated. These data are currently being used for the calibration of compressible LES[1] and RANS[2] turbulence models.

Introduction

The study of high-speed boundary layers is important in advancing supersonic and hypersonic flight technology. In a high-speed boundary layer, the kinetic energy is substantial and the dissipation due to the presence of the wall leads to large increases in the temperature. Therefore, a high-speed boundary layer differs from an incompressible one in that the temperature gradients are significant. Since the pressure remains nearly constant across the boundary layer, the density decreases where the temperature increases. Thus, to accommodate for an equivalent mass-flux, a supersonic boundary layer must grow faster than a subsonic one. The extra growth modifies the freestream, and the interaction between the inviscid freestream and the viscous boundary layer affects the wall-pressure distribution, the skin friction and the heat transfer. Furthermore, the high temperature in the boundary layer leads to air reactions. To improve our understanding of the flow physics and to calibrate turbulence models, we need accurate experimental and computational databases of high-speed flows.

Direct numerical simulations can provide a vast amount of accurate data that can be used to analyze turbulent boundary layers at high Mach numbers. Based on a better understanding of the real flow physics and using DNS data, accurate turbulence models for high-speed flows can be developed, calibrated and tested. Recent advances show that building a detailed DNS database of fundamental flows at supersonic and hypersonic conditions is attainable. For example, Guarini et al.[3] perform a DNS of a Mach 2.5 boundary layer at Re_θ=1577; Adams[4] performs a DNS of the turbulent boundary layer over a compression ramp at Mach 3 and Re_θ=1685; and Martin & Candler[5,6] perform DNS of reacting boundary layers at Mach 4. One of the achievements of this DNS work is the ability to accurately simulate turbulent flows at high Mach numbers while reproducing complex flow physics, shock waves and chemical non-equilibrium effects, permitting the study of turbulence under different flow conditions.

M	Re_θ	T_{wall}	Status
3	3000	isothermal	in progress
4	9480	adiabatic	completed
4	7225	isothermal	in progress
8	3600	isothermal	in progress

Table 1 Flow conditions and simulation status for the turbulent boundary layer database.

Studying physical phenomena via numerical and experimental databases requires controlled inflow conditions. This presents a challenge for numerical simulations since turbulent flows are highly non-linear and initialization procedures and simulation transients make the final flow conditions difficult to control.

In this paper, we present our progress in building a DNS database of hypersonic turbulent boundary layers. The governing equations and numerical method are first introduced. Then, we present an initialization procedure to minimize transients while matching the desired skin friction and Reynolds number. The Mach number, Reynolds number based on momentum thickness, and the wall temperature condition for the turbulent boundary layers are given in Table 1. Experimental data for the Mach 3 case are being gathered at the Gas Dynamics Laboratory in Princeton University. The experimental data for the Mach 8 boundary layer

	M_∞	ρ_δ	U_δ	$\theta \times 10^4$	$\mu_\delta \times 10^4$	ρ_w	u_τ	$\delta \times 10^3$	$\mu_w \times 10^4$
adiabatic	4	0.48	5684	3.66	1.06	0.132	270.25	6.5	2.90
isothermal	4	0.48	5798	2.70	1.04	0.507	147.00	3.42	1.01
adiabatic	0.3	1	104	1.70	0.18	1.0	4.69	1.51	0.18

Table 2 Dimensional boundary layer edge and wall parameters in SI units for the Mach 4 simulations.

is compiled in Baumgartner[7] and at present no experimental data is available for the Mach 4 conditions. Here, we describe the Mach 4 DNS data including the evolution from the initial condition to the realistic turbulent field and the estimated data accuracy. We then comment on the status of the more stringent Mach 8 DNS data.

Conserved equations for DNS

The equations describing the unsteady motion of a perfect gas flow are given by the mass, momentum, and total energy conservation equations

$$\frac{\partial \rho}{\partial t} + \frac{\partial}{\partial x_j}(\rho u_j) = 0,$$

$$\frac{\partial \rho u_i}{\partial t} + \frac{\partial}{\partial x_j}(\rho u_i u_j + p\delta_{ij} - \sigma_{ij}) = 0,$$

$$\frac{\partial \rho e}{\partial t} + \frac{\partial}{\partial x_j}\Big((\rho e + p)u_j - u_i\sigma_{ij} + q_j\Big) = 0,$$

where ρ is the density; u_j is the velocity in the j direction; p is the pressure; σ_{ij} is the shear stress tensor given by a linear stress-strain relationship

$$\sigma_{ij} = 2\mu S_{ij} - \frac{2}{3}\mu\delta_{ij}S_{kk},$$

where $S_{ij} = \frac{1}{2}(\partial u_i/\partial x_j + \partial u_j/\partial x_i)$ is the strain rate tensor, and μ is the temperature dependent viscosity and is computed using a power law; q_j is the heat flux due to temperature gradients

$$q_j = -\kappa\frac{\partial T}{\partial x_j} \ ,$$

where κ is the temperature dependent thermal conductivity; and e is the total energy per unit mass given by

$$e = c_v T + \tfrac{1}{2}u_i u_i,$$

where c_v is the assumed constant specific heat at constant volume.

Numerical Method

The numerical method combines a weighted essentially non-oscillatory (WENO) scheme for the inviscid fluxes with an implicit time advancement technique. The third-order accurate, high-bandwidth, WENO scheme was designed for low dissipation and high bandwidth[8] and provides shock-capturing, which is necessary at the Mach numbers that we consider. The time advancement technique is based on the Data-Parallel Lower-Upper (DPLR) relaxation method of Candler *et al.*[9] and was extended to second-order accuracy by Olejniczak & Candler.[10] The derivatives required for the viscous terms are evaluated using 4th-order central differences. We use supersonic boundary conditions in the freestream and periodic boundary conditions in the streamwise and spanwise directions. Thus, the boundary layer is develops temporally. The validity of periodic boundary conditions is briefly discussed in this paper. A more detailed discussion can be found in Xu & Martin.[11]

Flow Conditions

The freestream conditions are $M_\infty = 4$, $T_\infty = 5000$ K, and $\rho_\infty = 0.5$ kg/m^3. These conditions are representative of the boundary layer on a 26° wedge at a free-stream Mach number of 20 and 20 km altitude. The temperature in these simulations is chosen to be high so that the same simulations could be used to study the effect of chemical reactions.[5,6] The perfect gas assumption is used in the present study, which is intended to illustrate our initialization procedure and the accuracy of our simulations.

The Reynolds numbers based on the momentum thicknesses are 9480 and 7225 for the adiabatic and isothermal simulations, respectively. These Reynolds numbers correspond to a freestream velocity of 5708 m/s. The corresponding turbulent Reynolds numbers or Karman numbers, $Re_\tau = \rho_w u_\tau \delta/\mu_w$ where δ is the boundary layer thickness, . The values of Re_τ are 800 and 2450 for the adiabatic and isothermal simulations. For both cases, u_τ is two orders of magnitude larger than that of typical subsonic boundary layers. For the isothermal simulation the relatively higher density and lower viscosity values at the wall lead to a larger turbulent Reynolds number. The dimensional values that we use to compute these Reynolds numbers are given in Table2. For comparison, the values for a Mach 0.3 turbulent boundary layer computed in Martin *et al.*[12] are also provided. The Mach 0.3 DNS data compares well with experimental data.

T_w	δ^+	L_x/δ	L_y/δ	L_z/δ	Δx^+	Δy^+	N_x	N_y	N_z
adiabatic	800	6.5	1.6	11	13.5	5.1	384	256	128
isothermal	2450	3.7	0.9	14	24	9.2	384	256	150

Table 3 Grid resolution and domain size for the direct numerical simulations.

Resolution Requirements and Initialization

The mean velocity, density, and temperature profiles, and the inner parameters

$$u_\tau = \sqrt{\frac{\mu_w}{\rho_w}\left(\frac{\partial u}{\partial z}\right)_w}, \qquad z_\tau = \frac{\mu_w}{\rho_w u_\tau},$$

at the desired Mach number are being obtained from a Baldwin-Lomax Reynolds-averaged Navier-Stokes simulation[13] for the Mach 3 and Mach 8 cases. The Mach 4 initial mean profiles[12] for the present simulations were obtained from a k-ϵ RANS code and they did not match the law of the wall exactly. In turn, the simulations led to longer simulation transients to reach a statistically stationary state than those being obtained for the Mach 3 and Mach 8 cases. Notice that z is the normal direction. The fluctuating velocity field is obtained by normalizing the velocity fluctuations from the incompressible Mach 0.3 DNS[12] by the ratio of the inner parameters at the high Mach number to that at M =0.3. We have yet to determine the effect of using a Morkovin scaling for the fluctuating velocity. The turbulent field is mapped onto a computational domain that is also normalized in wall units. Thus, the initial turbulence structures and energy spectra resemble those of a realistic turbulent boundary layer. Our preliminary experience with the Mach 8 turbulent boundary layer simulations is that this initialization procedure may allow for short simulation transients provided that the mean turbulent profiles are accurate. The initial fluctuations in the thermodynamic variables are estimated using the strong Reynolds analogy.[14]

The DNS computational domain size and structured grid resolution required for the simulations is determined based on the characteristic large length scale, δ; the characteristic small, near-wall length scale, z_τ ; and grid convergence studies. The computational domain must be large enough to contain a good sample of the large scales. On the other hand, the grid resolution must be fine enough to resolve the near wall structures. The first requirement gives the size of the computational domain, whereas the later one gives an estimate on the grid resolution in wall units. Thus, increasing the ratio of the large to small scale δ/z_τ increases the required number of grid points. Ultimately, grid convergence studies or comparisons with experimental or semi-empirical data will determine the final resolution.

Let us consider the computational size and resolution estimates for the present simulations. From Table 2, the ratio of the large to small scales i.e. the Karman number $\delta^+ = \delta/z_\tau$, or turbulent Reynolds number Re_τ is 800 and 2450 for the adiabatic and isothermal simulations, respectively. Thus, the isothermal simulation will require a reduced number of grid points. To alleviate the resolution requirements for the isothermal simulation we use a shorter computational domain in both streamwise and spanwise directions, yet long enough to prevent correlation of the large scales. Also, if we were to use the same number of grid points per large structure for both simulations, the resolution would be coarser in wall units for the isothermal case. We apply this criteria, and we use slightly coarser resolution in wall units for the isothermal case. These constrains are relaxed for the adiabatic case. For both cases, the wall-normal grid is stretched. The first point away from the wall is located at $z^+ = 0.13$, and there are 21 grid points below $z^+ = 10$. The final domain size and grid resolution are given in Table 3. These correspond to meshes with $(384 \times 256 \times 128)$ and $(384 \times 256 \times 150)$ grid points in the streamwise, spanwise and wall-normal directions for the adiabatic and isothermal simulations, respectively. The consistency of the computational size is considered during the simulation by ensuring that the large structures in the inflow are not correlated with the large structures in the middle of the computational domain. The adequacy of the resolution in wall units is assessed via grid resolution studies and comparison with semi-empirical data.

By examining the two-point correlations, it was found that for the adiabatic simulation the lengths of 6.5δ and 1.6δ in the streamwise and spanwise directions, respectively, are adequate. For the isothermal simulation, 3.7δ and 0.9δ are sufficient. In the wall-normal direction, the height of the domain is set so that acoustic disturbances originating at the upper boundary do not interact with the boundary layer near the wall. The resulting grid spacing and resolution in each direction are given in Table 3. Note that although the resolution in wall units is coarser for the isothermal simulation, the resolution in outer units is nearly twice as large as it is for the adiabatic case.

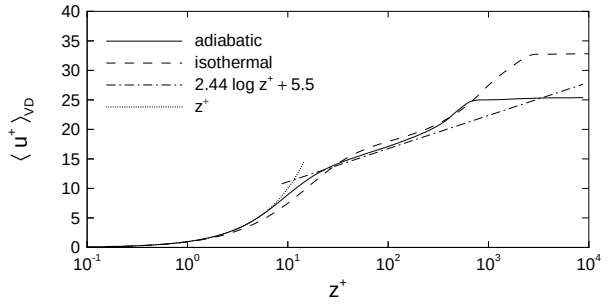

Fig. 1 Van-Driest transformed velocity profiles scaled on inner variables for the Mach 4 boundary layers.

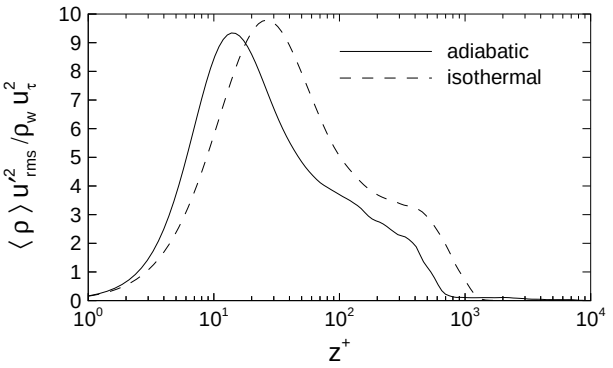

Fig. 2 Longitudinal turbulence intensity for the Mach 4 simulations.

Accuracy of the Mach 4 Turbulent Boundary Layer Data

The van Driest transformed velocity for the adiabatic and isothermal simulations nearly collapse up to the wake region as it is shown in Fig. 1. For the adiabatic simulation the intercept of the logarithmic layer is $C = 5.5$ and gives a value of u_τ that is underpredicted roughly by 8% when compared with the experimental value,[15] $C = 5.1$. For the isothermal simulation, the constant for the logarithmic region is $C = 6.6$. This simulation should be improved by modifying the resolution slightly in the near wall region.

Hopkins and Inouye[16] present a survey comparing different theories to predict the turbulent skin friction in supersonic and hypersonic boundary layers. They find that the van Driest II[17] theory gives the best prediction. For a given Re_θ, we compute C_f from the Kármán-Schoenherr equation given by

$$\frac{1}{F_c C_f} = 17.08[\log(F_\theta Re_\theta)]^2 + 25.11\log(F_\theta Re_\theta) + 6.012$$

where F_c and F_θ are van Driest II transformation functions computed as

$$\begin{aligned} F_c &= \frac{0.2rM_e^2}{(\sin^{-1}\alpha + \sin^{-1}\beta)^2}, \\ F_\theta &= \frac{\mu_e}{\mu_w}, \end{aligned}$$

where r is the recovery factor and α and β are calculated by

$$\begin{aligned} \alpha &= \frac{2A^2 - B}{\sqrt{4A^2 + B^2}}, \\ \beta &= \frac{B}{\sqrt{4A^2 + B^2}}, \end{aligned}$$

with

$$\begin{aligned} A &= \sqrt{\frac{0.2rM_e^2}{F}}, \\ B &= \frac{1 + 0.2rM_e^2 - F}{F}, \\ F &= \frac{T_w}{T_e}. \end{aligned}$$

For the adiabatic simulation, the predictions given by the DNS and the Van Driest II theory are within 2%. Hopkins *et al.*[18] find that the Van Driest II theory predicts the experimental data within about 10% error for $T_w/T_{aw} > 0.3$. For the isothermal simulation T_w/T_{aw} is about 0.26.

Figure 2 shows the longitudinal turbulence intensities using Morkovin scaling. The peak value for the isothermal simulation is slightly overestimated probably due to the underprediction on u_τ. The adiabatic simulation agrees well with the incompressible predictions. The turbulent kinetic energy budget for the adiabatic simulation is shown in Fig. 3. We observe that the turbulent kinetic energy transfer mechanisms resemble those of a Mach 2.5 adiabatic DNS.[3] These findings allow us to be confident in the quality of the data.

Figure 4 shows the two-dimensional energy spectra for the more challenging isothermal simulation. The spectra have been obtained by averaging in time and in planes parallel to the wall for $z^+ = 975$, 145, and 7, respectively. The grid resolution can be assessed using the value of $k_{\max}\eta$, where $k_{\max}$ is the maximum wave number and η is the Kolmogorov length scale. We find that $k_{\max}\eta$ varies from 0.3 near the wall to 1.2 in the wake. These values have been found adequate in previous numerical simulations.[3,19] Figure 5 shows the two-point correlations for the same simulation. There correlations converge to small values in the spanwise direction near the edge of the boundary layer. Thus, the domain size is marginally large enough to enclose an adequate sample of the large

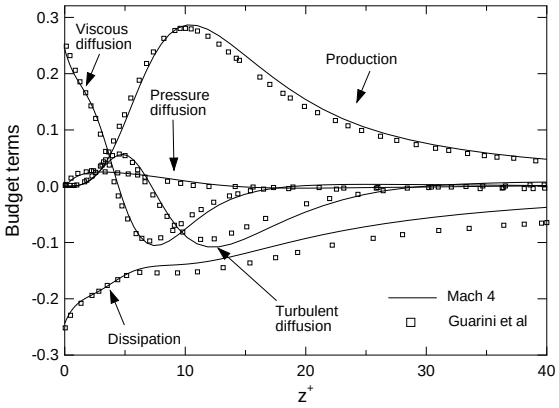

Fig. 3 Turbulent kinetic energy budget for the adiabatic case.

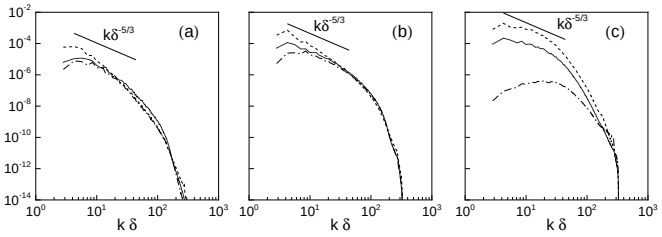

Fig. 4 Two-dimensional energy spectra at (a) $z^+ = 975$, (b) $z^+ = 145$, and (c) $z^+ = 7$ for the isothermal simulation. ---- streamwise, ····· spanwise and —·— wall-normal velocity component.

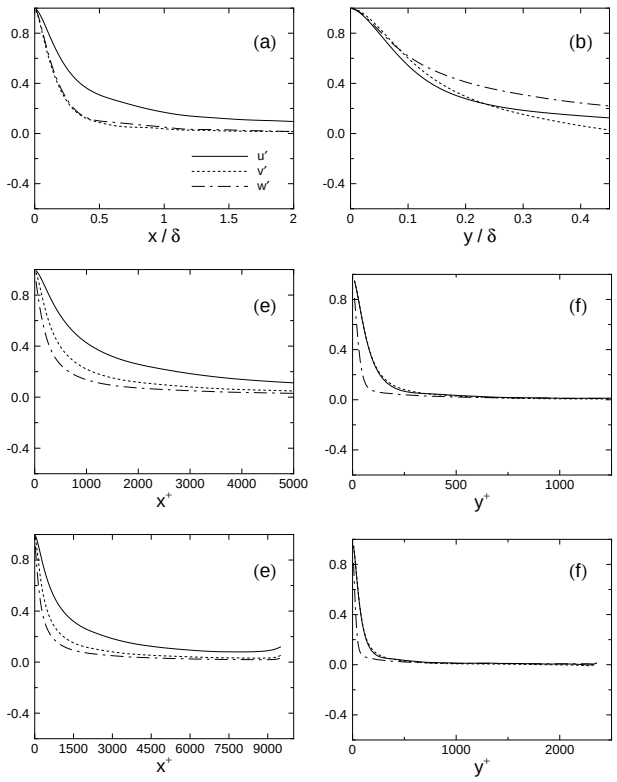

Fig. 5 Two-point correlations at (a)-(b) $z^+ = 975$, (c)-(d) $z^+ = 145$, and (e)-(f) $z^+ = 7$ for the isothermal simulation. ---- streamwise, ····· spanwise and —·— wall-normal velocity component.

turbulent structures in the wake region. In the logarithmic and near wall regions, the correlations are negligible. Note that the small correlation that appears near the wall in the streamwise direction is expected. Both computations[20] and experiments[21] have shown that the near-wall streaky structures are more coherent in the streamwise direction for high Mach numbers. The same degree of correlation is found for the adiabatic simulation, where the domain size is 1.7 times longer than that of the isothermal case in the streamwise direction.

Periodicity and statistical convergence

The amount of energy that is present in a supersonic boundary layer and the small computational domains that are used in the present simulations, make it possible to use periodic boundary conditions in the streamwise direction. A time developing boundary layer simulation is valid provided that (i) the flow can be considered quasi-steady, i.e. the flow adjusts to its local (in time) conditions much faster than the boundary layer thickness changes, and (ii) for the purposes of gathering statistics, the time sampling is shorter than the time scale for boundary layer growth. A flow that satisfies these conditions evolves slowly and can be viewed as a good approximation of a static station of a boundary layer.

The growth time, adjusting time, and sampling time can be estimated as

$$t_{\text{growth}} = \left(\frac{1}{\overline{\delta}} \frac{d\overline{\delta}}{dt} \right)^{-1} , \quad t_\Lambda = \frac{\overline{\delta}}{U_e} , \quad t_{\text{sample}} = \frac{\overline{\delta}}{\overline{u}_\tau} ,$$

respectively. Where $\overline{\delta}$ and $\overline{u}_\tau$ are the averaged boundary layer thickness and wall friction velocity and U_e is the velocity at the edge of the boundary layer. For the simulations, t_Λ is at least two orders of magnitude smaller than t_{growth}, and t_{sample} is less than t_{growth}. Thus, the temporal development of the boundary layer is negligible during an appropriate data collection time. These premises have been further corroborated in Xu and Martin[11] by comparing temporal and extended temporal simulation results for the adiabatic Mach 4 simulation.

It should be noticed that it is necessary to initialize the boundary layer to a nearly equilibrium state for realization of these conditions. If the initial flow field is far from equilibrium, a long temporal transient develops before the flow settles down to a quasi-stationary state. In this scenario, the final skin friction and the

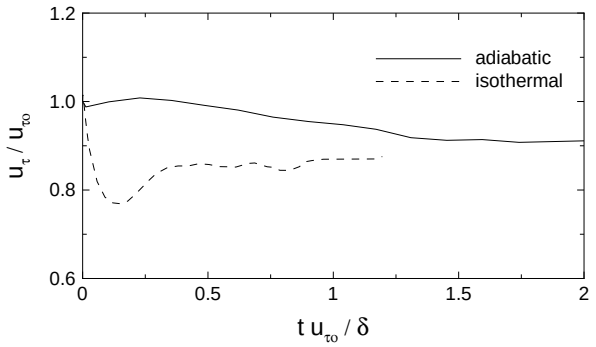

Fig. 6 Temporal evolution of the friction velocity.

Reynolds number are hard to control.

Figure 6 shows the temporal evolution of the friction velocity u_τ normalized by its initial value. The time is made non-dimensional by $u_{\tau o}/\delta$. For the adiabatic simulation, u_τ reaches a stationary state in about 1.3 periods of time. For the isothermal simulation, u_τ reaches a stationary value after about $0.3tu_{\tau o}/\delta$. All statistics are computed in time and space during one $u_{\tau o}/\delta$ period of time after the simulations reach the statistically stationary state.

The statistics were gathered in space and time in over fifty large-eddy turnover characteristic times, δ/U_e, and included thirty three computational boxes.

Shockwaves and Shocklets

Experimental data[21–23] have shown that the turbulence structure in a boundary layer is very similar for incompressible and compressible flows. As in the Mach 2.5 DNS data of Guarini *et al.*,[3] the Mach 4 turbulent statistics are very similar to those found in incompressible boundary layers. In this section we focus on the compressibility effects and the differences between the adiabatic and isothermal simulations, for which the maximum fluctuating Mach number $(M - \langle M \rangle)$ is 0.35 and 0.30, respectively.

An index of the compressibility is given by

$$\chi = \frac{\langle\ |\nabla \cdot \mathbf{u}'|^2\ \rangle}{\langle\ |\nabla \times \mathbf{u}'|^2\ \rangle}\ ,$$

which represents the amount of turbulent kinetic energy in the compressible modes of motion relative to the amount of incompressible turbulent kinetic energy. Figure 7a shows that in the near wall region, the ratio of compressible to incompressible energy is as large as 0.13 and 0.15 for the adiabatic and isothermal simulations, respectively. Figure 7b shows a large increase in the value of χ near the boundary layer edge. This result indicates the possible presence of shocks in the outer part of the boundary layer. since a jump in χ indicates a jump in the compressible dissipation $(\frac{4}{3}\nabla\cdot\mathbf{u}')$.

The predominant mechanism for the generation of shock waves in these flows occurs when slow moving,

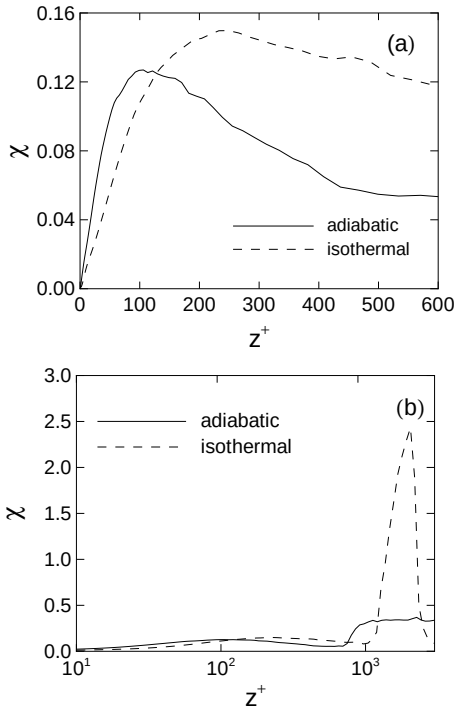

Fig. 7 Relative compressible to incompressible energy ratio (a) near the wall and (b) near the boundary layer edge.

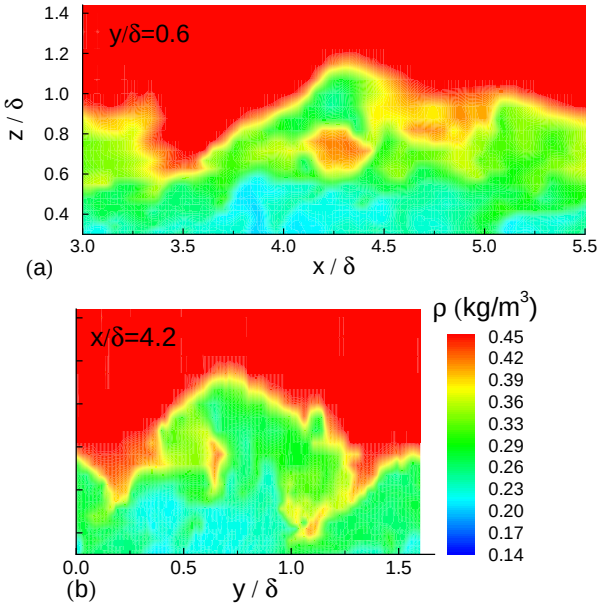

Fig. 8 Density contours on the (a) streamwise-wall-normal and (b) spanwise-wall-normal plane for the adiabatic direct numerical simulation.

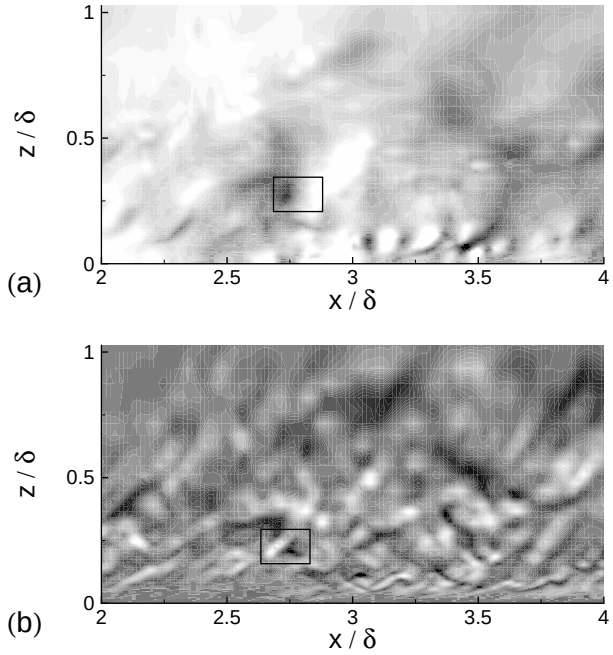

Fig. 9 Contours of (a) pressure and (b) divergence of the velocity on a streamwise-wall-normal plane for the adiabatic simulation.

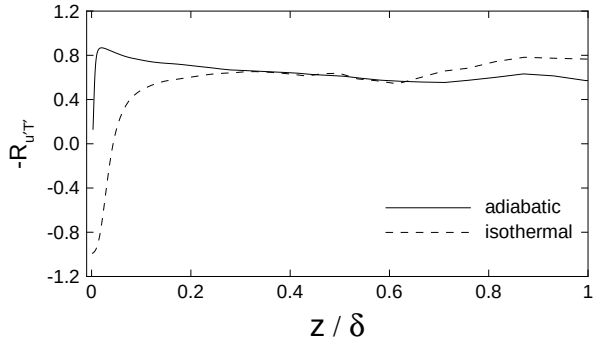

Fig. 10 Fluctuating streamwise velocity and temperature correlation coefficient.

near-wall gas is lifted into the high-speed outer flow. Such a bursting event is illustrated in Figure 8, which shows the density in a streamwise/wall-normal plane and a spanwise/wall-normal plane. Note that the low-speed gas has a significantly higher temperature and lower density than the outer region gas, and thus the burst event is easily identified by the low density regions.

Detecting the location of shock waves in this flow is very difficult. Following the approach of Blaisdell *et al.*,[24,25] we search for locations of large compression and streamwise increase in the static pressure. We then sample the data along instantaneous streamlines upstream and downstream of the candidate shock location and compute the upstream relative Mach number, M_1^{rel}, using

$$u_1 - u_2 = a_1 M_1^{rel} - a_2 M_2^{rel}$$

where the downstream relative Mach number, M_2^{rel}, is a known function of M_1^{rel}. The variables u_1, u_2, a_1, and a_2 are pre- and post-shock velocity and speed of sound obtained from the simulation data. We find that there tends to be very little deflection of the flow across most of the candidate shock waves, so we use normal shock relations to obtain M_2^{rel}. Once we have found the relative Mach number of the shock, we can compute the pressure rise across the shock and compare it to the DNS data.

Figure 9 plots contours of pressure and divergence in a streamwise/wall-normal plane. The highlighted region shows the location of a candidate shock wave. Sampling the data at the upstream and downstream conditions, we find that the shock wave has a relative Mach number of about 1.10. This gives a pressure rise that is consistent with the data, and we conclude that there is indeed a shock wave in this region. Again, because of the complicated interaction between the near-wall gas and the outer flow, the identification of the pre- and post-shock conditions is difficult. Thus, it is not possible to calculate the exact shock Mach number.

We have found shock waves in regions closer to the wall than that illustrated above. For the adiabatic boundary layer, the maximum shock Mach number is about 1.12. From Figure 9, it is clear that the highlighted shock wave has a small length scale, with a wall-normal dimension of only about 0.03δ. This is characteristic of the other shock waves that we have identified in the simulation data.

Since the amount of compressible energy is significant in the logarithmic and boundary layer edge regions, the transport of turbulent kinetic energy due to sound radiation (acoustic waves) must be addressed. An index of such interaction is the correlation coefficient for the streamwise-velocity and temperature fluctuations $-R_{u'T'}$. Figure 10 plots this correlation coefficient. For the adiabatic simulation, $-R_{u'T'}$ is always positive since the mean gradients of velocity and temperature are of opposite sign. For the same simulation, $-R_{u'T'}$ peaks at 0.9 near the wall. For the isothermal simulation, $-R_{u'T'}$ is -1.0 at the wall where the mean temperature and velocity gradients are of the same sign. For this simulation, the turbulent Reynolds number is high and the boundary layer edge is characterized by an energized turbulent wake. Thus, near the boundary layer edge where most of the turbulent kinetic energy is in the compressible modes, $-R_{u'T'}$ increases. For both simulations, $-R_{u'T'}$ is near 0.6 for $0.3 \leq z/\delta \leq 0.7$, as it is for incompressible flows. This result is also consistent with the DNS data of Guarini *et al.*[3] for a flat plate at a free-stream Mach number

of 2.5.

Gaviglio[26] postulated that a possible mechanism that contributes to maintaining the magnitude of $R_{u'T'}$ within the boundary layer is the small-scale internal intermittency of turbulence due to compressibility. Here we have seen that for the isothermal simulation, $R_{u'T'}$ is maintained in the wake due to the large-scale intermittency of the wake and compressibility. However, elsewhere within the boundary layer, $R_{u'T'}$ follows the trend of the incompressible flow data.[26] Thus, no effect of the small-scale intermittency due to compressibility is observed in the present study. The ratio of compressible to incompressible turbulent kinetic energy away from the boundary layer edge is about 0.15 for the present simulations. For the conditions chosen, the local compressibility effects are not substantial enough to counteract the de-localization provided by vortical pressure fluctuations. Experimental data shows no effect of the shockwaves or shocklets in the dynamics of compressible boundary layers at Mach numbers up to 8,[7,27] except for a reduction in the length scale.[28]

Effect of Wall Temperature on Energy Transfer

After having examined the effects of compressibility, we will consider the turbulent energy mechanisms. There are four energy exchange mechanisms that take place in turbulent boundary layers: transport, production, dissipation and diffusion of turbulence. The budget equation for the turbulent kinetic energy is

$$\frac{\partial}{\partial t}(\overline{\rho}\,\widetilde{k}\,)+\widetilde{w}\frac{\partial}{\partial z}(\overline{\rho}\,\widetilde{k}\,) = P+T+\Pi_t+\Pi_d+\phi_{dif}+\phi_{dis}+ST$$

where

$$\begin{aligned}
P &= -\overline{\rho u_i'' w''}\;\frac{\partial \widetilde{u}_i}{\partial z}\;, \\
T &= -\frac{1}{2}\;\frac{\partial}{\partial z}\overline{\rho u_i'' u_i'' w''}\;, \\
\Pi_t &= -\frac{\partial}{\partial z}\overline{w'' p'}\;, \qquad \Pi_d = \overline{p'\frac{\partial u_i''}{\partial x_i}}\;, \\
\phi_{dif} &= \frac{\partial}{\partial z}\overline{u_i'' \sigma_{i2}'}\;, \qquad \phi_{dis} = \overline{\sigma_{ij}'\frac{\partial u_i''}{\partial x_j}}\;, \\
ST &= -\overline{w''}\frac{\partial \overline{p}}{\partial z} + \overline{u_i''}\frac{\partial \overline{\sigma_{ij}}}{\partial x_j} - \overline{\rho}\,\overline{k}\,\frac{\partial \widetilde{w}}{\partial z}\;, \qquad (1)
\end{aligned}$$

and P is the production due to the mean gradients, T is the redistribution or transport of turbulent kinetic energy, Π_t is the pressure diffusion, Π_d is the pressure dilatation, ϕ_{dif} is the viscous diffusion, ϕ_{dis} is the viscous dissipation, and the ST represents a group of small terms. The first two appear due to the difference between the Favre and Reynolds averaging, the third one is the dilatation-production term.

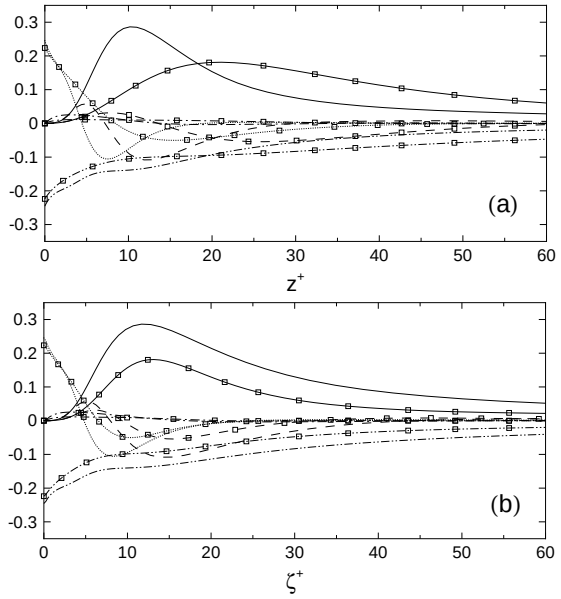

Fig. 11 Turbulent kinetic energy budget (a) Traditional coordinate transformation; (b) Mathematical coordinate transformation including the variation of the thermodynamic variables; ——— production; ····· viscous diffusion; —·— pressure diffusion; – – – – transport; —··— viscous dissipation. The lines denote the adiabatic case, lines and symbols the isothermal one. The variables have been made nondimensional using $u_\tau \sigma_w / z_\tau$, where $\sigma_w = \rho_w u_\tau^2$.

Figure 11a shows the terms in the budget of the turbulent kinetic energy for the adiabatic and isothermal wall simulations under the traditional coordinate transformation. Figure 11b shows a better collapse of the data when using a coordinate transformation that takes into account the variation in density and temperature across the layers. This transformation is given by

$$\zeta^+ = \int_0^z \frac{\langle\rho\rangle u_\tau}{\langle\mu\rangle}\;dz.$$

The magnitude of turbulent kinetic energy production, viscous diffusion and viscous dissipation are larger for the adiabatic case. The location of the maximum and minimum values for the turbulent kinetic energy transport term is nearly the same for both simulations when plotted versus ζ^+. Similar to incompressible flows, the rest of the terms in the turbulent kinetic energy transport equation are negligible for both cases. Being consistent with the supersonic simulations of Huang[3] and Coleman,[29] we find that the dissipation is nearly solenoidal.

Let us now consider the vorticity in the flow field. The total change of vorticity can be written as

$$\frac{D\vec{\omega}}{Dt} = (\vec{\omega}\cdot\nabla)\,\vec{u} - \vec{\omega}\,(\nabla\cdot\vec{u}) + \nabla T \times \nabla S\;,$$

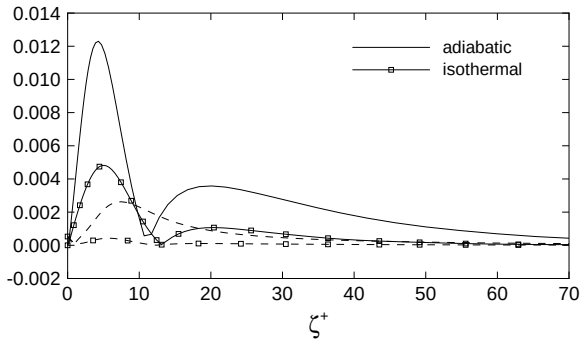

Fig. 12 Normalized amplitude of vorticity production terms for the adiabatic and isothermal simulations. ——— stretching/tilting and - - - - compressibility term. The variables have been made nondimensional using u_τ and z_τ.

where $\vec{\omega}$ and $\vec{u}$ are the vorticity and velocity vectors respectively, T is the temperature and S is the entropy. The first term on the right hand side is the production of vorticity due to vortex stretching and tilting mechanisms, the second term is due to the compressibility of the flow, and the third term is due to the change in the thermodynamic variables and includes the baroclinic torques.

Figure 12 shows the magnitude of the stretching/tilting and compressibility terms for the simulations. The compressibility term is dominant near $\zeta^+ = 12$ for the adiabatic simulation, and negligible for the isothermal case. For both simulations, the baroclinic torque is negligible in comparison to the stretching/tilting mechanism.

The different wall temperature conditions have different effects on the mean variables, which in turn lead to differences in the turbulent structures. In particular, the wall-cooling is a sink of energy, thus there is more energy dissipated for the isothermal wall simulation than for the adiabatic case. It is the difference in the mean velocity gradient that affects the location of the buffer-region structure and the turbulence production and dissipation mechanisms. For the isothermal case, the increased magnitude of the stretching/tilting term relative to the compressible term indicates that the structures are more elongated than for the adiabatic simulation. Also, since the vortex stretching/tilting and turbulent kinetic energy mechanisms take place farther from the wall, the near-wall region is more quiescent for the isothermal simulation.

These results are consistent with the flow structure topology shown in Fig. 13, where the structures are visualized using iso-surfaces of the second invariant of the velocity gradient tensor Φ.[30] In Figures 13a and 13b the domain is given in δ units to identify the large structures for the adiabatic and isothermal simulations. Comparing these two figures, we observe that

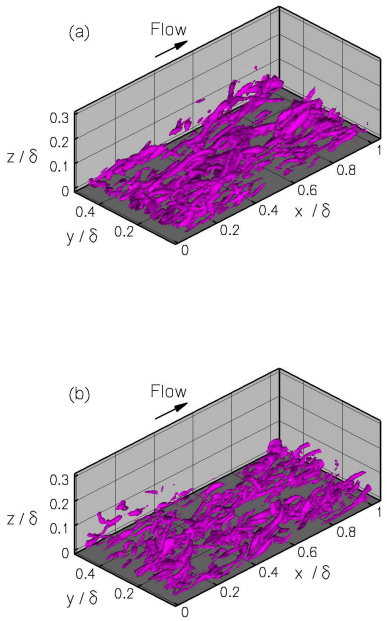

Fig. 13 Flow structure visualized using iso-surfaces of Φ with 0.001% of the maximum value for the (a) adiabatic and (b) isothermal simulations with coordinates in δ units.

when plotted in this fashion the structures are larger for the adiabatic simulation.

Figures 14a and 14b plot iso-surfaces of Φ in a domain that is normalized in wall units, $x_i^+ = x_i/z_\tau$. We observe that the structures are larger for the isothermal simulation. This result is consistent with the fact that δ^+ increases with decreasing wall temperature. For the adiabatic simulation, the turbulence structures look similar when plotted in a domain measured in either δ or z_τ units. In contrast, for the isothermal simulation, the flow structure topology differs substantially depending on whether we choose freestream or wall units to nondimensionalize the domain.

Conclusions

We present an initialization procedure that leads to short simulation transients, which is necessary to control the final skin friction and Re_θ for the simulation. We applied this procedure to initialize adiabatic and isothermal turbulent boundary layers. We are in the process of testing the repeatability of the initialization in Mach 3 and Mach 8 boundary layers.

The preliminary Mach 4 adiabatic and isothermal turbulent boundary layer data are presented. The comparison with available experimental and computational data shows that the adiabatic simulation data are accurate, and the resolution for the isothermal case should be and will be increased for a more accu-

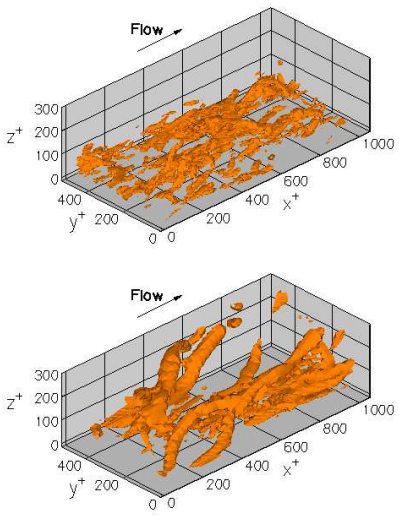

Fig. 14 Flow structure visualized using iso-surfaces of Φ with 0.001% of the maximum value for the (a) adiabatic and (b) isothermal simulations with coordinates in z_τ units.

rate representation of the friction velocity. Ensuring that periodic boundary conditions are adequate requires performing simulations in short computational domains. At present, we have not assessed the adequacy of the large scale computational sample and whether the amount of energy computed represents that of a statistical sample containing a large enough number of structures. We are conducting this study by relaxing the periodic boundary condition assumption and using the inflow boundary conditions of Xu & Martin.[11]

The bursting events that are present in a turbulent boundary layer bring low-momentum fluid from the near wall toward the boundary layer edge, and large-scale compression regions form where the low-speed fluid meets the incoming freestream. We find that the compressibility ratio is a good index of the location of these regions and that shock waves are present in the Mach 4 boundary layers. The average Mach number of the shocks is about 1.10 and the wall-normal dimension is about 0.03δ. As observed experimentally,[7,27] the shock structures have no effect on the overall dynamics of the turbulent boundary layers.

The effect of wall temperature is studied. We find a better collapse of the turbulent kinetic energy and vorticity budgets when the wall coordinate is modified to take into account the changes in the thermodynamic variables. The cold-wall boundary condition for the isothermal simulation is a sink of energy. Thus, the magnitude of the turbulence mechanisms such as production and dissipation of turbulent kinetic energy are smaller than those in the adiabatic simulation. The vorticity budgets show an increased magnitude of the stretching/tilting term relative to the compressibility term for the isothermal simulation. This is consistent with the structures being more elongated for the isothermal case. As δ^+ increases with decreasing wall temperature, the structures plotted in wall units are larger for the isothermal case.

These data will be available to the community.

Acknowledgments

We would like to thank NASA Ames for the use of the DPLR CFD code to generate the turbulent mean flow, and to Michael Wright at ELORET for his guidance in how to use this code. We would also like to thank Datta Gaitonde for making us aware of existing semi-empirical data for the validation of the Mach 4 boundary layer simulations. This work was supported by the Air Force Office of Scientific Research under grant AF/F49620-02-1-0361 and the National Science Foundation under grant # CTS-0238390.

References

[1]Martin, M., "Shock-capturing in LES of high-speed flows," *Center for Turbulence Research, Annual Research Briefs 2000*, 2000, pp. 193–198.

[2]Sinha, K. and Candler, G., "Turbulent dissipation-rate equation for compressible flows," *AIAA Journal*, Vol. 41, 2003, pp. 1017–1021.

[3]Guarini, S., Moser, R., Shariff, K., and Wray, A., "Direct numerical simulation of supersonic turbulent boundary layer at Mach 2.5," *Journal of Fluid Mechanics*, Vol. 414, 2000, pp. 1–33.

[4]adams, N., "Direct simulation of the turbulent boundary layer along a compression ramp at $M = 3$ and $Re_\theta = 1685$," *Journal of Fluid Mechanics*, Vol. 420, 2000, pp. 47–83.

[5]Martin, M. and Candler, G., "DNS of a Mach 4 boundary layer with chemical reactions," *AIAA Paper No. 2000-0399*, 2000.

[6]Martin, M. and Candler, G., "Temperature fluctuation scaling in reacting boundary layers," *AIAA Paper No. 2001-2717*, 2001.

[7]Baumgartner, M., "Turbulence structure in a hypersonic boundary layer," *Ph.D. Thesis, Princeton University*, 1997.

[8]Weirs, V. and Candler, G., "Optimization of weighted ENO schemes for DNS of compressible turbulence," *AIAA Paper No. 97-1940*, 1997.

[9]Candler, G., Wright, W., and McDonald, J., "Data-Parallel Lower-Upper Relaxation method for reacting flows," *AIAA Journal*, Vol. 32, 1994, pp. 2380–2386.

[10]Olejniczak, D. and Candler, G., "Hybrid finite-difference methods for DNS of compressible turbulent boundary layers," *AIAA Paper No. 96-2086*, 1996.

[11]Xu, S. and Martin, M., "Inflow boundary conditions for the simulation of compressible turbulent boundary layers," *AIAA Paper No. 2003-3963*, 2003.

[12]Martin, M., Olejniczak, D., Weirs, G., and Candler, G., "DNS of reacting hypersonic boundary layers," *AIAA Paper No. 98-2817*, 1998.

[13]DPLR, CFD, and Code, *NASA Ames Research Center, Moffett Field, CA*, 2003.

[14]Morkovin, M., "Effects of compressibility on turbulent flows," *A.J. (ed) of Mèchanique de la Turbulence, CNRS*, 1962, pp. 367–380.

[15]Fernholz, H. and Finley, P., "A critical commentary on mean flow data for two-dimensional compressible boundary layers," *AGARDograph*, Vol. 253, 1980.

[16]Hopkins, E. and Inouye, M., "An evaluation of theories for predicting turbulent skin friction and heat transfer on flat plates at supersonic and hypersonic Mach numbers," *AIAA Journal*, Vol. 9, 1971, pp. 993–1003.

[17]Driest, E. V., "Problem of aerodynamic heating," *Aeronautical Engineering Review*, Vol. 15, 1956, pp. 26–41.

[18]Hopkins, E., Rubesin, M., Inouye, M., Keener, E., Mateer, M., and Polek, T., "Summary and correlation of skin-friction and heat-transfer data for a hypersonic turbulent boundary layer," *TN D-5089 NASA*, 1969.

[19]Kim, J., Moin, P., and Moser, R., "Turbulence statistics in fully developed channel flow at low Reynolds number," *Journal of Fluid Mechanics*, Vol. 177, 1987, pp. 133–166.

[20]Coleman, G., Kim, J., and Moser, R., "Numerical study of turbulent supersonic isothermal-wall channel flow," *Journal of Fluid Mechanics*, Vol. 305, 1995, pp. 159–183.

[21]Spina, E., Smits, A., and Robinson, S., "The physics of supersonic turbulent boundary layers," *Annual Review of Fluid Mechanics*, Vol. 26, 1994, pp. 287–319.

[22]Spina, E. and Smits, A., "Organized structures in a compressible, turbulent boundary layer," *Journal of Fluid Mechanics*, Vol. 182, 1987, pp. 85–109.

[23]Smith, M. and Smits, A., "Visualization of the structure of supersonic turbulent boundary layers," *Experiments in Fluids*, Vol. 18, 1995, pp. 288–302.

[24]Blaisdell, G., Mansour, N., and Reynolds, W., "Numerical simulations of compressible homogeneous turbulence," *Thermosciences Division, Department of Mechanical Engineering, Stanford University*, Vol. Report No. TF-50, 1991.

[25]Blaisdell, G., Mansour, N., and Reynolds, W., "Compressibility effects on the growth and structure of homogeneous turbulent shear flow," *Journal of Fluid Mechanics*, Vol. 256, 1993, pp. 443–485.

[26]Gaviglio, J., "Reynolds analogies and experimental study of heat transfer in the supersonic boundary layer," *International Journal of Heat and Mass Transfer*, Vol. 30, 1987, pp. 911–926.

[27]

[28]Smits, A. and Dussauge, J., *Boundary Layer Mean-Flow Behavior*, AIP PRESS, 1996, In Turbulent Shear Layers in Supersonic Flows.

[29]Huang, P., Coleman, G., and Bradshaw, P., "Compressible turbulent channel flows," *Journal of Fluid Mechanics*, Vol. 305, 1995, pp. 185–218.

[30]Blackburn, H., Mansour, N., and Reynolds, W., "Topology of finite-scale motions in turbulent channel flow," *Journal of Fluid Mechanics*, Vol. 310, 1996, pp. 269–292.